Received: 5 April 2022 | Revised: 26 May 2022 | Accepted: 26 June 2022 | Published on: 2 August 2022

DOI: 10.1002/mrm.29390

RESEARCH ARTICLE

Magnetic Resonance in Medicine

A *z*-gradient array coil with a dedicated active-shielded array coil for MRI

Manouchehr Takrimi[1] | **Ergin Atalar**[1,2]

[1]National Magnetic Resonance Research Center (UMRAM), Bilkent University, Ankara, Turkey

[2]Department of Electrical and Electronics Engineering, Bilkent University, Ankara, Turkey

Correspondence
Manouchehr Takrimi, National Magnetic Resonance Research Center (UMRAM), Bilkent University, 06800 Bilkent, Ankara, Turkey.
Email: mtakrimi@bilkent.edu.tr

Purpose: An array-based *z*-gradient coil with a set of programmable power amplifiers can outperform a conventional *z*-gradient coil and make it highly customizable with a broader range of tunable features.

Methods: A dynamically adjustable imaging volume can be achieved using a pair of independent arrays and a modified optimization procedure based on analytic equations. Two modes of operation are provided: (a) standard mode that resembles a conventional coil; (b) advanced mode, where all performance parameters can be adjusted employing a controllable feeding mechanism. Commercial software is used to demonstrate the validity and feasibility of the proposed coil.

Results: Primary and shield array diameters are 24 and 30 cm, both of which comprise 12 bundles of 10 turns copper wires. Maximum feeding voltage/current is 250 V/100 A for all array elements. Four distinct magnetic profiles are provided: (a) conventional profile with 140 mm diameter spherical region of interest, 120 mT/m gradient, and up to 4500 T/m/s slew rate; (b) profile of 200 mT/m, 70 mm region of interest, and up to 6900 T/m/s slew rate; (c) 60 mm axially shifted 70 mm region of interest with 120 mT/m strength and 3600 T/m/s slew rate; and (d) profile of 370 mT/m, 120 mm region of interest, and 3700 T/m/s slew rate when the active shield is reverse fed.

Conclusion: By using an active-shielded gradient array coil, the magnetic field profile of the imaging volume can be adjusted dynamically, and it can provide new features and a wide range of field profiles for diverse applications in MRI.

KEYWORDS

active shield, array coil, gradient coil, magnetic profile, tunable imaging volume

1 | INTRODUCTION

Gradient array coils, also known as "multi-coil gradients" or "matrix gradient coils," have recently been used for diverse applications, including spatial encoding; field profiling; shimming of B_0 field; and for some cases, a combination of them. In Ref.[1], a set of individual circular coils is used to generate linear and more complex gradient fields within an arbitrary region of interest (ROI).

This approach permits the simultaneous generation of the encoding and shimming fields by the same setup. No shielding exists in this design.

In, Ref.[2], an optimization problem is formulated to achieve local nonlinear encoding and eddy current reduction, resulting in novel coil elements for an actively shielded matrix gradient coil. Although the proposed plan offers an active shield, the shield current cannot be independently controlled. Another actively shielded gradient array coil is given in Ref.[3], consisting of 84 independent channels. It is achieved by designing 2 different coil elements, which form a cylindrical coil configuration that contains 2 primary current-carrying surfaces and a shared shielding surface. It is shown that the proposed structure can flexibly generate encoding fields. Finally, in Ref.[4], an optimized version of the last 2 works is proposed with a reduced number of gradient power amplifiers (GPAs) due to the circuit's complexity. Recently reported array-based coils[5–11] are also very flexible in generating customized magnetic fields, but either there is no shield or the shield coil is not independent. The benefits of the proposed active-shielded z-gradient array configuration, thanks to its shield independence, are twofold:

1. In its standard mode of operation, both the primary and shield arrays can be programmed to serve as a conventional z-gradient coil with usual functionality and performance parameters.
2. In its advanced mode of operation: (a) both of the arrays can be controlled dynamically using a suitable set of driving currents to adjust the performance parameters and control the overall magnetic profile within the ROI; (b) the shield array functionality can be manipulated to accompany the primary coil and increase the gradient strength or adjust the slew rate.

The overall field profile in both modes of operation is based on a modified optimization procedure accompanied by a set of stringent constraints on the performance parameters. These constraints guarantee that: (a) the profile variation has either a negligible effect on the performance parameters, or at least its possible effects are controllable; (b) necessary shielding is always available when switching between different modes. Furthermore, without compromising the warm bore's temperature and degrading the field profile due to induced eddy currents, the advanced mode of operation makes it possible:

a To tune the gradient strength, the slew rate, and the field linearity,
b To adjust the shape, longitudinal position, and dimension of the ROI that best suits the application,

In this work, we focus on the feasibility of an active-shielded z-gradient array coil. This feasibility study is on a small animal size coil. The proposed design provides a dynamic imaging volume with a highly flexible field profile.

2 | METHODS

Using an analytic expression, the longitudinal vector component of the magnetic flux density, $\overline{B}$, generated by a filamentary circular current loop is calculated. A coaxial arrangement of these loops along the coil axis can be used to calculate the total magnetic flux density and then design the z-gradient array coil.

2.1 | Magnetic flux density calculation

Because the wire pattern for a z-gradient coil is composed of coaxial circular annular wires, it is crucial to calculate the exact $\overline{B}$ field generated by a planar current loop (on the xy-plane) at an arbitrary distance from its center. The longitudinal component of the magnetic flux density, B_z, created by a filamentary circular wire loop of current I and radius a, at an arbitrary point of height h and radial distance ρ, from its center is given by Ref.[12]:

$$B_Z(a,\rho,h) = \frac{\mu I}{2\pi\sqrt{(a+\rho)^2+h^2}} \times \left[K(k) + \frac{\left(a^2-\rho^2-h^2\right)}{(a-\rho)^2+h^2}E(k)\right]; \quad k^2 = \frac{4a\rho}{(a+\rho)^2+h^2}, \tag{1}$$

where K and E are the complete elliptic integrals of the first and second kinds. Using Equation [1], the overall longitudinal magnetic flux density B_z for the z-array coil can be calculated using superposition. We assume that the primary array coil consists of N_C bundles of annular wire loops of current $A_{C,m}, m = 1 \ldots N_C$. The wire bundles are uniformly spaced along the z-axis with an inter-bundle gap of b_C, where each bundle contains M_C turns of uniformly distributed wire loops with an interwire gap of g_C, as shown in Figure 1A. Additionally, the bundles are symmetric with respect to the xy-plane. The diameter and length of the primary coil are shown by d_C and l_C, respectively. Similar naming is used to refer to the shield array parameters by replacing the index "C" with "S" as $N_S, M_S, g_S, b_S, r_S, l_S$, and $A_{S,n}, n = 1 \ldots N_S$. The main reason for a uniform spacing is because the intended dynamic ROI faces almost a similar structure and coil arrangement when it is shifted along

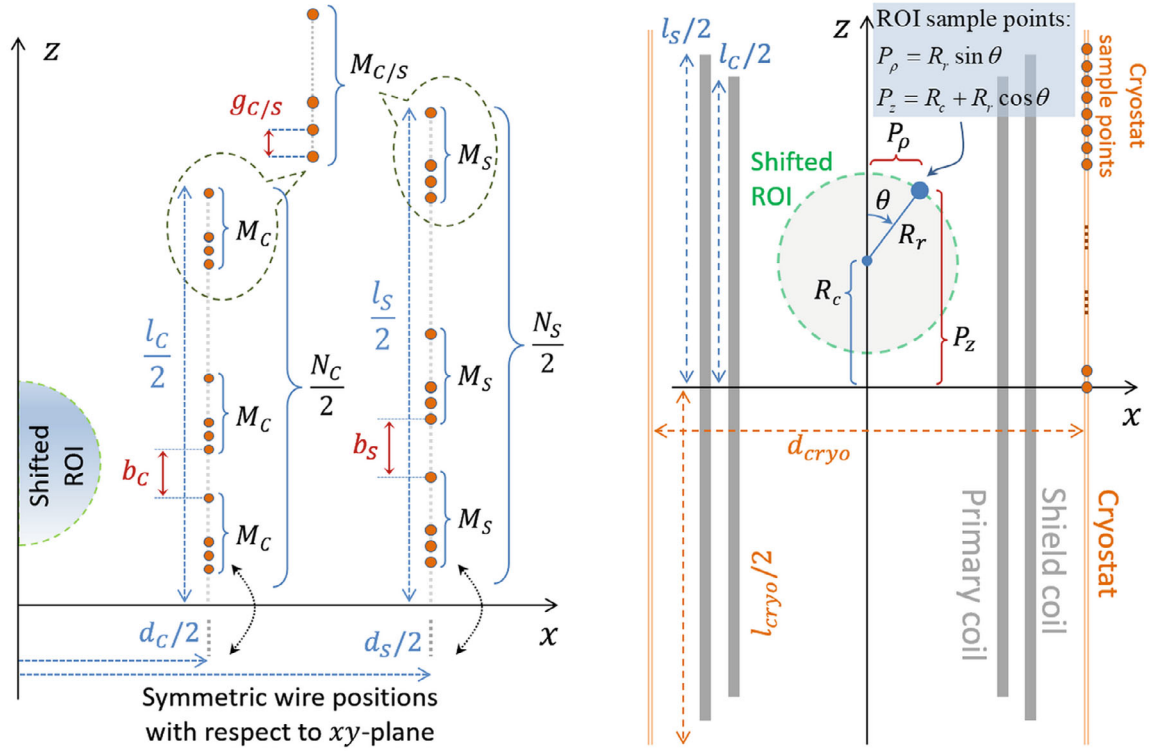

FIGURE 1 (A) A quarter cross-section of the proposed z-array coil consisting of the inner primary array and outer shield array, where tiny circles show the wire positions. d_C, l_C and d_S, l_S are the diameter and length of the primary and shield arrays, respectively. The interwire gaps are shown by g_C and g_S, and the interbundle gaps are shown by b_C and b_S. Wires in other quadrants are in symmetrical positions with respect to the relevant axes. (B) The cross-section view for both the primary and the shield arrays, the shifted ROI, and the cryostat, showing the relative positions and corresponding parameters. R_c and R_r are the ROI center and radius, respectively. The TPs on the border of the ROI (P_ρ, P_z) are controlled by the angle θ from 0 to π. The TPs along the cryostat are also shown by tiny circles. ROI, region of interest; TP, target points.

the coil axis; hence, the expected coil performance can be significantly preserved by adjusting the feeding currents.

By deploying the symmetry about the xy-plane, the wire positions $W_{C,m}$ on the primary array and $W_{S,n}$ on the shield array can be found. Given the radii of both coils, the overall longitudinal magnetic flux density B_{Array} at any arbitrary point (ρ, z) inside and outside of the coil (except within the wires) can be written as:

$$\begin{aligned} &B_{\text{Array}}\left(A_C, A_S, \rho, z\right) \\ &= \sum_{m=1}^{N_C M_C} A_{C,\lceil m/M_C \rceil} B_Z\left(r_C, \rho, z - w_{C,m}\right) \\ &+ \sum_{n=1}^{N_S M_S} A_{S,\lceil n/M_S \rceil} B_Z\left(r_S, \rho, z - w_{S,n}\right), \end{aligned} \tag{2}$$

where "⌈⌉" is the ceil function. Equation [2] involves 3 sets of variables:

1. Integer variables N_C and N_S, both of which should be determined based on the available GPAs for the primary and the shield arrays.
2. Integer variables M_C and M_S that may be determined based on the required maximum field strength and the expected shield effectiveness.
3. Real variables A_C and A_S, which are calculated by introducing a cost function and performing an optimization routine to achieve a specific field profile.

2.2 | The coil dimensions

The field strength decreases rapidly when the array elements get farther from the isocenter. This effect becomes dominant for the far-end array elements when the ROI is close to the other end. It means that the array should be as short as possible to get the most out of their generated fields. Assuming a conventional $\{x, y, z\}$ layer sequence for both the primary and the shield coils, the diameter and length of the shield array is chosen to be $d_S = 30$ cm and $l_S = 35$ cm, respectively, which is a proper size for small animal imaging. Considering 10 mm thickness for each coil layer, the primary/shield coil diameter for the x-and y-gradient coils would be 20/26 cm and 22/28 cm,

respectively; and the diameter of the primary z-gradient array must be $d_C = 24$ cm. To achieve stronger primary fields within the shifted ROIs and also create better shielding when the shifted ROI is close to either of both ends, we choose the primary array length to be 5 cm less than the dedicated shield array length, that is, $l_C = 30$ cm. Additionally, in order to mimic the existence of the cryostat's warm bore and its possible effects, an aluminum cylindrical shell of $d_{Cryo} = 90$ cm diameter, $l_{Cryo} = 80$ cm height, 10 mm thickness, and conductivity of 3.8×10^7 S/m has been inserted into all simulations.

2.3 | The constraints

Because the array dimensions are known, some geometrical, practical, electrical, and method-oriented constraints should be considered to design the proposed array coil as follows:

1. Geometrical constraints: Considering the wire diameter d_w, interwire gaps $g_{C/S}$, interbundle gaps $b_{C/S}$, number of bundles $N_{C/S}$, and number of wires per bundle $M_{C/S}$, the total length of the windings should be less than the dedicated lengths $l_{C/S}$. Additionally, $g_{C/S} \geq d_w$ to prevent any overlapping. The interbundle gaps should be at least twice the wire diameter, that is, $b_{C/S} \geq 2d_w$ to separate the bundles and attach the external wires.
2. Practical constraints: It is better to consider appropriate grooves for all wires on the formers. Depending on the construction accuracy, the minimum distance between 2 adjacent grooves should be at least a few tenths of a millimeter. It makes the wire positions accurate and prevents wire displacements due to winding errors. Additionally, it stops wires sliding under the applied forces and continuous vibrations.
3. Electrical constraints: (a) The maximum driving current for all bundles is limited to $|A_{C/S}| \leq I_{max}$; (b) the maximum driving voltage is limited to V_{max}.
4. Method-oriented constraints: Because we deploy a modified version of the target field method using discrete windings,[13] some constraints should be enforced for B_{Array} at the target points (TPs). Part of these TPs are defined on/inside the ROI(s) to achieve the required shape, position, linearity, and gradient strength; and the remaining TPs should be considered on the (cylindrical) surface of the cryostat's warm bore.

The proposed array coil is circularly symmetric about the z-axis and, hence, a shifted polar coordinate system is deployed to address the TPs and integrate the constraints into a mathematical expression suitable for the optimization. This approach effectively helps to minimize the linearity errors due to position-shifting or shape-scaling. Figure 1B illustrates the cross-sectional view of the proposed array coil showing the primary coil, shield coil, cryostat, and related parameters. In this figure, R_c and R_r are the center and radius of the shifted ROI (in green), respectively, and θ controls the angular position of TPs on the boundary. Additionally, the TPs along the cryostat are shown. To have a more complete picture of the final design with the dimensions already given, Figure 2 shows the partial cross-section view of a hybrid gradient system composed of a quarter of the x- and y-gradient coils and half the proposed z-gradient array, which is the subject of this work.

2.4 | Practical considerations

Using Figure 1A, one can show that for a single layer of winding, there is a binding relation among the parameters mentioned in the first constraint as:

$$N_C (M_C - 1) g_C + (N_C - 1) b_C + d_w \leq l_C, \tag{3}$$

Equation [3] shows a nonlinear relation among the geometrical parameters that dictates the wire positions on both arrays. Note that B_{Array} in Equation [2] is a linear function of the driving currents $A_{C/S}$; however, at the same time it is a nonlinear function of wire positions and also 4 integer parameters. Complicated tradeoffs exist between N_C, M_C, and the field profiles. A similar argument goes for the shield array. The complication increases dramatically when an acceptable shift in the ROI position is required, whereas the other performance parameters (linearity, gradient strength, shield effectiveness) should remain intact. As a general solution to tackle the problem, a mixed-integer nonlinear optimization problem with a set of linear and nonlinear constraints should be defined and solved to achieve the expected field profile that may or may not have a feasible solution. We deploy a few practical considerations to choose proper values for the integer variables, which in turn eliminate the need for mixed-integer optimization and reduces the complexity:

(a) The maximum rating of the 24 available GPAs in our lab is 250 V/100 A. To keep the balance between the magnetic fields created by both array coils, we prefer to choose $N_C = N_S = 12$.
(b) The need for a high gradient strength means that M_C (the number of wire turns per each bundle) should be as large as possible. Taking into account less than 25% duty cycle for driving GPAs, 2 mm diameter

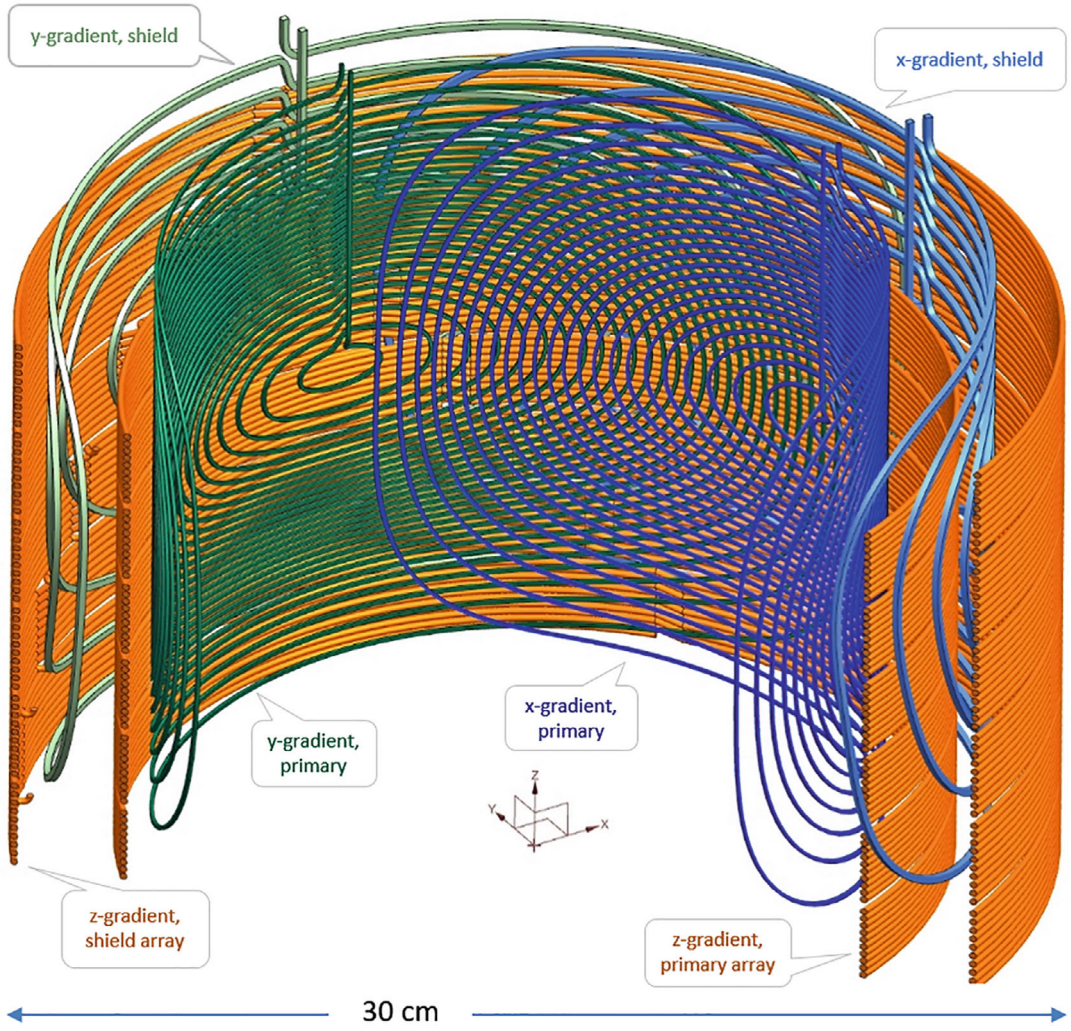

FIGURE 2 The partial cross-section view of a hybrid gradient system composed of half the proposed *z*-gradient array and a quarter of the *x*- and *y*-gradient coils. The *z*-gradient array consists of 2 sets of 12 wire bundles, each with 10 copper wires of 2 mm diameter. The diameter/height of the primary and the shield array coils are 24/30 and 30/35 cm, respectively. The diameter of the primary/shield coil for the *x*- and *y*-gradient coils are 20/26 cm and 22/28 cm, respectively. An aluminum cylindrical shell of 90 cm diameter, 800 mm height, and 10 mm thickness has been used for all simulations to mimic the existence of the cryostat, but it is not shown here.

copper wire would be a rational choice for the windings. Considering 30 cm coil length, 2 mm wire diameter, 12 bundles of 2 mm physical distance in between, and about 0.2 mm gap between consecutive grooves, the number of wires per bundle will be $M_C = 10$.

(c) Because the shield array is 5 cm longer, M_S may be different than M_C. Choosing $M_S < M_C$ increases the current burden on the shield array GPAs when the primary coil elements are driven close to the maximum current. On the other hand, choosing $M_S \geq M_C$ provides better shielding effectiveness and needs less currents to achieve the same performance parameters; however, the larger dimension of the shield array elements and a higher number of turns increases the impedance (especially the inductance) dramatically compared to the primary array elements. Choosing $M_S = M_C$ keeps a balance between the maximum available slew rate (driving speed) and the performance parameters. We provide a comparison for 2 different values of M_S in the first design example.

2.5 | Optimization procedure

To achieve a precise control over the uniformity of the field gradient within the ROI, especially when it is shifted, we deploy a series of distinct constraints on and inside the ROI for every TP rather than the usual method, which is the sum of squared field deviations. This approach reduces the optimization problem to a linear least square problem with $(N_C + N_S)$ unknown feeding currents A_C and A_S, where

the total B_{Array} field has to be minimized on the surface of cryostat. The final form of the linear least square problem reads:

$$\min_{A_C, A_S} \left\{ \sum_{p=-N_{\text{cryo}}}^{N_{\text{cryo}}} B^2_{\text{Array}} \left(A_C, A_S, \rho_{\text{cryo}}, h_p \right) \right\}, \tag{4}$$

subjected to the following constraints:

$$\begin{cases} \frac{1}{B^{\max}_{\text{ideal}}} \left| B_{\text{Array}} \left(A_C, A_S, R_r \sin\theta_n, R_c + R_r \cos\theta_n \right) \right. \\ \quad \left. - G_z R_r \cos\theta_n \right| \le \varepsilon_{\text{ROI}}, & n = 1 \cdots N_{\text{ROI}} \\ \frac{1}{B^{\max}_{\text{ideal}}} \left| B_{\text{Array}} \left(A_C, A_S, 0, R_c + z_m \right) - G_Z z_m \right| \le \varepsilon_{\text{ROI}}, \\ \qquad\qquad\qquad\qquad m = -N_Z \cdots N_Z \\ \left| A_{C,i} \right| \le I^{\max}, & i = 1 \cdots N_C \\ \left| A_{S,j} \right| \le I^{\max}, & j = 1 \cdots N_S \end{cases} \tag{5}$$

where $I^{\max} = 100$ A in this work; G_Z is the desired gradient intensity such that $B^{\max}_{\text{ideal}} = G_z R_r$ is the expected maximum B_{Array} field within the ROI; and B_{Array} is defined in Equation [3]. N_{ROI} is the number of TPs on the right semicircle boundary of the ROI, where $\theta_n = \pi \left(\frac{n}{N_{\text{ROI}}} \right)$ controls the angular position of the points when n goes from 1 to N_{ROI} (as shown in Figure 1B). N_Z is the half number of TPs along the z-axis and inside the ROI, where $z_m = R_r \left(\frac{m}{N_Z} \right)$ controls the points' positions from $-R_r$ to R_r when m goes from $-N_Z$ *to* N_Z. Inside the cost function, N_{cryo}, is the half number of TPs along the cryostat surface, and $h_p = l_{\text{cryo}} \left(\frac{p}{2N_{\text{cryo}}} \right)$ spans the longitudinal distance of $-l_{\text{cryo}}/2$ to $l_{\text{cryo}}/2$ when p goes from $-N_{\text{cryo}}$ to N_{cryo}. The tuning coefficient, ε_{ROI}, controls the maximum field linearity error on and inside the (shifted) ROI, and its typical value is between 5% to 15%. Note that a similar set of constraints may be defined to achieve nonspherical ROI(s) for different applications. Furthermore, a better shielding control may be obtained by assigning more TPs close to the area where the (shifted) ROI is located.

The first set in [5] enforces N_{ROI} distinct constraints that guarantee the relative field deviations on the (shifted) ROI will not exceed ε_{ROI}. Simulations show that choosing at least 3 ($N_Z = 1$) and at most 5 ($N_Z = 2$) points inside the (shifted) ROI helps achieving a better linearity. This is controlled by the second constraint that inserts extra $2N_Z + 1$ TPs inside the (shifted) ROI to have a linearity deviation no more than ε_{ROI} along the z-axis. It helps to search for a better gradient uniformity inside the ROI within all possible solutions that could be a local minimum. These constraints should be duplicated for as many ROIs as needed. It should be emphasized that the above optimization problem is defined to guarantee a predefined level of linearity error while minimizing the stray fields close to the cryostat region. It can be modified to guarantee a predefined level of shielding effectiveness while maximizing the field linearity.

Taking into account the maximum degrees of freedom that we may have in such an optimization problem, it is possible to estimate how many TPs (for both of the ROI and the cryostat region) should be considered to get acceptable results that satisfy the above-mentioned constraints. We have 24 independent currents to be determined. In the standard mode of operation, the coil is symmetric about the origin, and at most 12 degrees of freedom exist. However, in the advanced mode of operation, 24 degrees of freedom exist, and more TPs have to be considered for a smooth and satisfactory convergence of the optimization problem given in Equation [4] and its constraints in Equations [5]. Because at least 3 to 5 TPs are inside the ROI, 20 points on the boundary of the ROI ($N_{\text{ROI}} \le 20$) would be enough to run the optimization. The same scenario is valid for the cryostat region, except that for shifted ROIs a few more points deliver more satisfactory results. In this work, we choose $N_{\text{cryo}} \le 27$ for different simulations provided in the result section. The nonlinear programming solver command (*NLPSolve*) of Maple 2021[14] software is deployed to carry out these optimizations due to its flexibility in programming and capability in using analytic expressions for both the cost function and the constraints. An Intel CORE-i7 Eighth Generation laptop with 12GB of memory and Windows 10 operating system is utilized to carry out all simulations. All of the optimizations in the results section take at most 120 s to converge.

2.6 | Error estimation

Due to multiple exponentially decaying time constants governing the induced eddy currents, the overall gradient field generated by both applied and induced currents deviates from the expected ideal waveform.[15] The better the shielding, the shorter the time required for the magnetic fields to settle down toward their ideal waveforms dictated by the applied trapezoidal currents. In this work, there are 12 distinct set of time constants for 24 symmetrically positioned wire bundles along the z-axis that are fed independently and synchronously by trapezoidal waveforms of 100 μs rise/fall time and 300 μs plateau time. Because less eddy-induced fields mean better shielding and faster field settling, we define the gradient field settlement error (GFS):

$$\text{GFS}(\%) = \left| \frac{B_Z(\tau \text{ seconds after the fall time})}{B_Z(\text{before the fall time})} \right| \times 100 \tag{6}$$

as a figure-of-merit to compare different field profiles without involving above mentioned time constants. Based on the transient simulations carried out to assess the GFS error, it is observed that (a) choosing $\tau = 100$ μs is a reasonable choice; (b) it is almost insensitive to the sampling location (as long as it is inside the ROI and has a non-zero axial coordinate). The sampling point is chosen in the first quadrant (due to symmetry) at an oblique angle of $\theta = 45^{\circ}$ about the z-axis and half distance from the center to the boundary of the ROI.

On the other hand, the uniformity of the field gradient within the shifted ROI is assessed by Ref.[8]:

$$\mathrm{err}\,(\%) = 100 \times \max_{\mathrm{ROI}} \left| \frac{B_{\mathrm{Array}} - G_Z\,(z - R_C)}{B_{\mathrm{ideal}}^{\mathrm{max}}} \right|, \qquad (7)$$

where z is the absolute height of the field probing point on and inside the ROI. Note that for multiple ROIs and shifted cylindrical or shifted disk-shaped ROIs,[16] the interior of the ROI should be included for the error assessment because maximum field deviation does not always happen on the boundary. A tunable planar disk makes it possible to achieve a higher gradient strength when imaging a slice.

It is worthwhile to emphasize that we use current sources[17] instead of voltage sources to feed the array elements and carry out the electromagnetic simulations. The voltages developed at the terminals of 24 array elements are determined by the resistance of the coils and complicated electromagnetic interactions among the wire bundles (24 self and 94 distinct mutual inductances) and the induced currents within the cylindrical body of the warm bore. For all upcoming simulations, the maximum power loss due to eddy currents, maximum ohmic power loss within the array coils, maximum achievable field slew rate, and maximum voltages across the array elements (comprised of both the resistive and induced voltages) will be provided for further insight and comparison.

3 | RESULTS

The proposed array-based z-gradient coil has two modes of operation: In the standard mode, its overall functionality is comparable with a conventional z-gradient coil of similar performance parameters. For this reason, the simulation of a conventional z-gradient coil with almost the same performance parameters is provided for comparison without including the design details because there are publications in this field.[13] However, the advanced mode provides some extended features that are not available in other publications; hence, no comparison is provided. The numerical simulations presented in this work are based on Ansys Maxwell 2019.R1.[18] It should be emphasized that for all of provided numerical simulations, the proximity effect for the copper wire bundles is ignored for the sake of simplicity.

3.1 | Standard mode: ROI at the center of the coil

We commence by describing a design where the proposed array is deployed as a conventional z-gradient coil. Figure 3 shows the optimized feeding currents for both the primary and the shield arrays. In this figure, the red/blue dots show the longitudinal position and the positive/negative values of the feeding currents. The RMS value of 24 feeding currents is 61.6 A. These currents are imported to the Ansys Maxwell to verify the design approach. The B_z field plot is shown in Figure 4 for peak input current at $t = 400\ \mu s$. A gradient strength of 120 mT/m at the center of 140-mm diameter spherical ROI with an efficiency of 1.95 mT/m/A_{rms} and 10% deviation from linearity can be seen. Additionally, the B_z field transient simulation at the field sampling point is provided at the bottom of the same figure, where m1 and m2 marker values for both horizontal (X) and vertical (Y) axes are reported inside the table. These values indicate a GFS error of 2×10^{-6}% defined in Equation [6]. Two other field transient simulations (not shown in the figure) indicated a maximum of 13.4 μW power loss due to induced eddy currents inside the cryostat, and a maximum of 4.1 kW ohmic power loss in both the primary and shield array elements. The self-inductance and resistance of array elements are 47 μH and 46 mΩ for the primary array and 60 μH and 58 mΩ for the shield array elements. The maximum voltage across all array elements during 100 μs ramp-up time is 66 V. Considering the available 250 V GPAs, a maximum of 4580 T/m/s field slew rate is achievable.

As mentioned in section 2.4, a larger number of wire turns (M_{S}) for shield elements can be used. A set of similar simulations for $M_{\mathrm{S}} = 13$, instead of $M_{\mathrm{S}} = 10$, show almost the same performance parameters except the maximum eddy power loss, which reduces to 2.3 μW due to a better shielding; and total ohmic power loss, which increases to 4.47 kW due to increased resistance. However, 83% reduction for maximum eddy power loss and almost 10% increase in ohmic power loss are achieved at the cost of increased impedance for the shield array elements. The inductance for $M_{\mathrm{S}} = 13$ is 101 μH, 70% higher than the one for $M_{\mathrm{S}} = 10$, and almost 2.1 times larger than the inductance for the primary array element. Regarding the resistance, it reads 79 mΩ, which is 40% larger than the case for $M_{\mathrm{S}} = 10$ and 70% larger than the resistance of

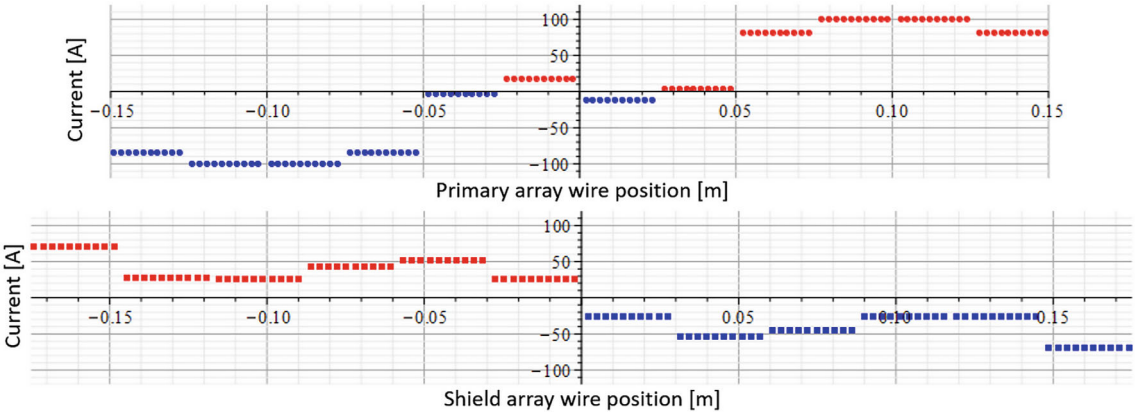

FIGURE 3 The optimized feeding currents for both the primary and the shield arrays when the proposed array is used in the standard mode as a conventional z-gradient coil. The red/blue dots (circle for primary and square for shield) show the longitudinal position and the positive/negative values of the feeding currents along the horizontal and vertical axes, respectively. The RMS value for 24 feeding currents is 61.6 A.

FIGURE 4 The geometrical setup and the B_z field plot of the proposed array, deployed as a conventional z-gradient coil. Both of the primary and shield arrays and the spherical ROI are shown. The number of wire bundles and the number of wires per bundle is 12 and 10 for both coils, respectively. A 10 mm thick cylindrical aluminum cryostat of 90 cm diameter is shown by a vertical gray strip at the rightmost of the picture. The contour lines indicate 1 mT separations. Additionally, the B_z field transient simulation at the field sampling point is provided, where m1 and m2 marker values are given for both time (X) and field (Y) axes in the table. A gradient strength of 120 mT/m with an efficiency of 1.95 $\mathrm{mT/m/A_{rms}}$ and a 10% deviation from linearity can be seen within the ROI of 140 mm diameter. The GFS error (using m1 and m2 marker values) is less than 2.0×10^{-6}%. Active shielding performance can be seen between the shield array and the cryostat. GFS, gradient field settlement.

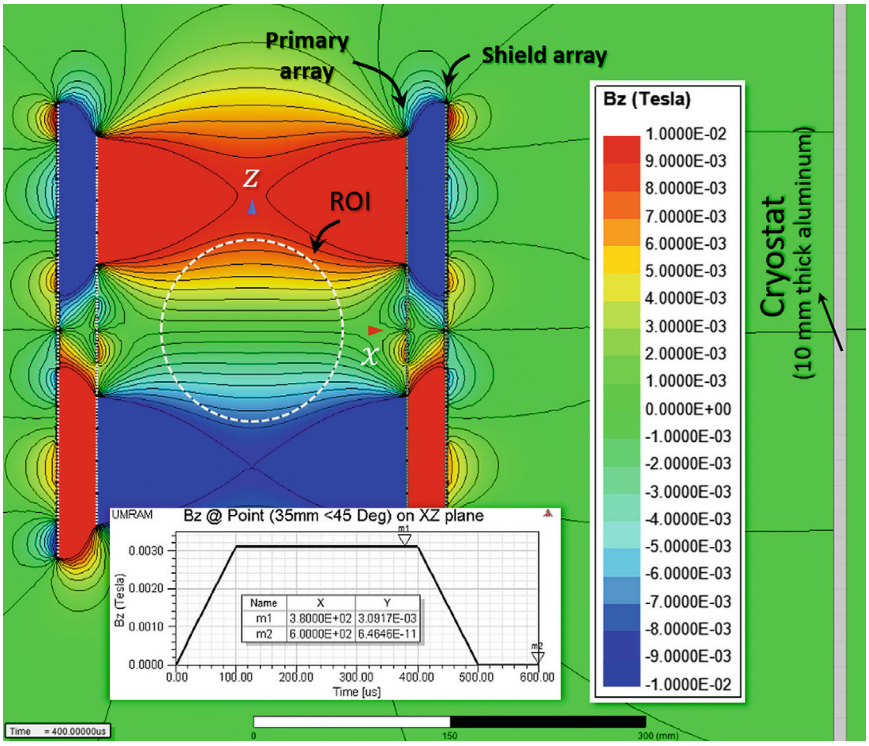

the primary array elements. These higher values of inductance and resistance reduces the available slew rate in the advanced mode of operation.

3.2 | Conventional *z*-gradient coil, a comparison study

The standard mode of operation acts as a conventional *z*-gradient coil. To have a comparison, a conventional active-shielded z-gradient coil with almost the same performance parameters, composed of 34 (primary coil) and 20 (shield coil) circular annular wires of 2 mm diameter, is designed using Maple. The same simulation conditions consisting of a trapezoidal current source of 95 A amplitude as well as similar rise and fall times are used. Figure 5A shows 54 wire positions for both the primary (blue circles) and the shield (red squares) coils. Figure 5B illustrates half of the coil, both primary and shield coils, the ROI, half B_Z field plot, and the space between the coil and cryostat, where the contour lines indicate 1 mT separations. Simulations (not shown in the figure) indicate

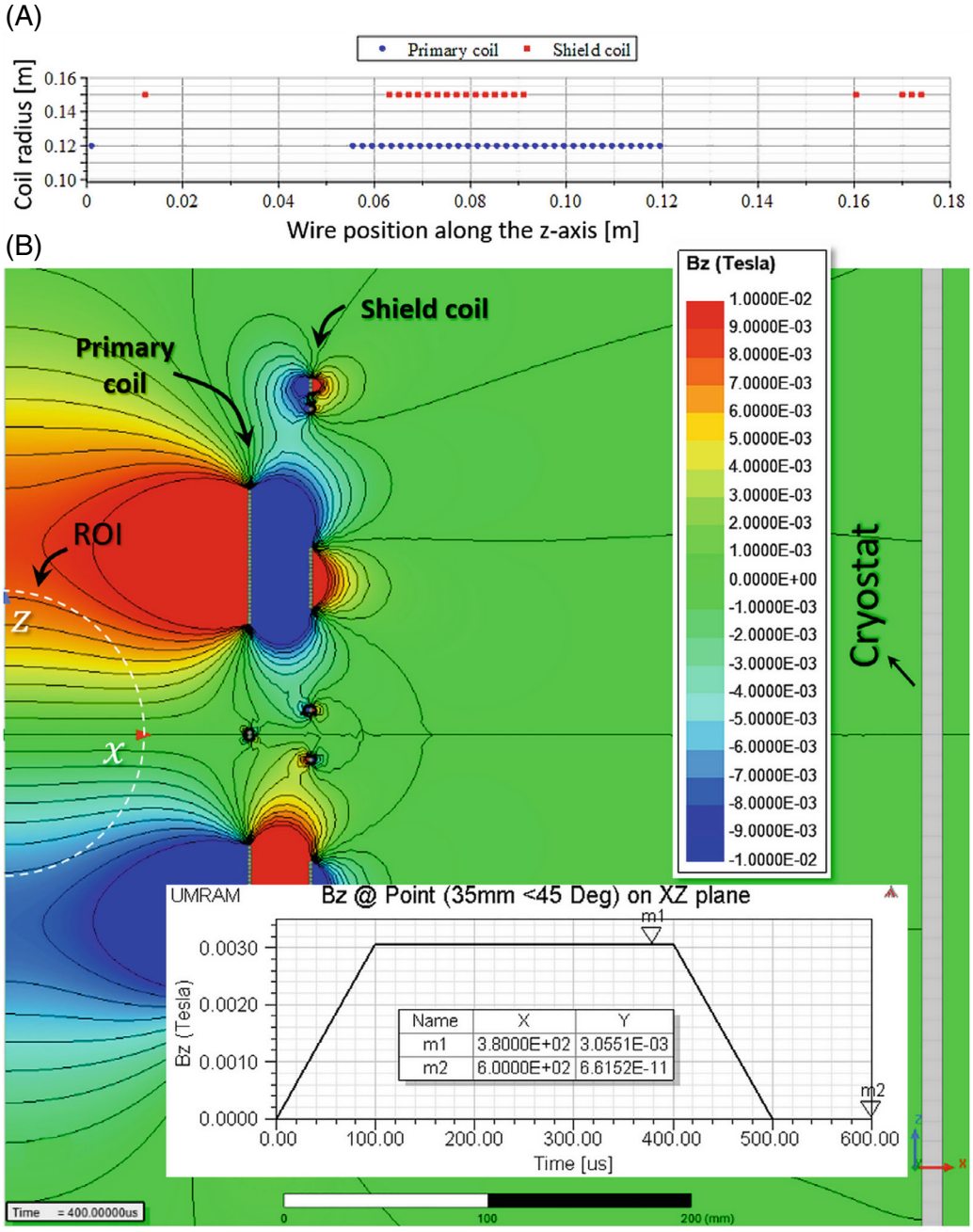

FIGURE 5 The structure and field simulation of a conventional z-gradient coil consisting of 34 and 20 circular annual wires of 2 mm diameter for the primary and shield coils, respectively. (A) The calculated axial wire positions: blue circles for the primary coil of 12 cm radius, red squares for the shield coil of 15 cm radius. (B) The half B_z field plot of the conventional z-gradient coil. Both of the primary and shield coils and the 140 mm spherical ROI are shown. The cryostat is shown at the rightmost of the picture. The contour lines show 1 mT separations. (C) The B_z field transient response at the field sampling point where m1 and m2 marker values are given for both time (X) and field (Y) axes in the table. The actuating current is 94.6 A. A gradient strength of 121 mT/m with an efficiency of 1.27 mT/m/A and a 16.1% deviation from linearity can be seen within the ROI. The GFS error is less than 2.1×10^{-6}%.

a maximum of 0.68 μW power loss due to induced eddy currents inside the cryostat, and a maximum of 4.71 kW ohmic power loss in both coils. The actuating current is 94.6 A. A gradient strength of 121 mT/m at the center of 140 mm diameter ROI, efficiency of 1.27 mT/m/A, and 16% deviation from linearity is seen. An explanation about possible reasons for a lower efficiency (compared to array case) is given in the discussion. The inset Figure 5C shows the B_Z field transient response at the same sampling point. The GFS error is about 2.1×10^{-6}%, which is equal to the array case. The inductance and resistance of the conventional coil are 494 μH and 530 mΩ, respectively. The

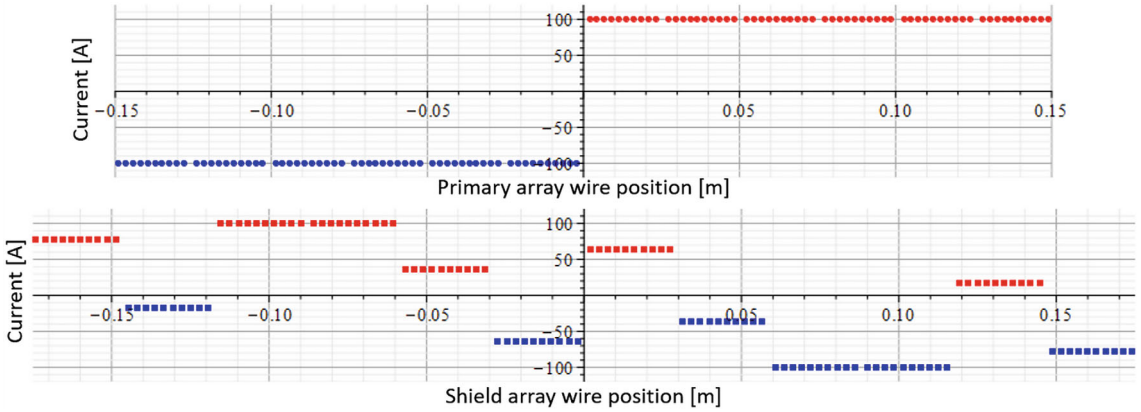

FIGURE 6 The optimized feeding currents for the first example in the advanced mode for both the primary and the shield arrays explained in section 3.3. The red/blue dots (circle for primary, square for shield) show the longitudinal position and the positive/negative values of the feeding currents along the horizontal and vertical axes, respectively. The RMS value for 24 feeding currents is 87.3 A.

maximum voltage across the coil during the ramp-up time is 517 V, which is more than 7 times higher than the arrays example.

3.3 | Advanced Mode: 70% higher gradient with a smaller ROI at the center

As the first array design in the advanced mode, the gradient strength increases by 70% to 206 mT/m. Due to a trade-off between performance parameters, the ROI diameter is reduced by 50% to 70 mm to maintain the field's linearity and the expected shielding effectiveness based on the GFS error. The B_z field plot for a new set of optimized feeding currents shown in Figure 6 is depicted in Figure 7 without showing the fields around the cryostat. The RMS value of currents is increased by 12%, reaching 87.3 A, which provides an efficiency of 2.36 mT/m/A_{rms}. Simulations show an 8% deviation from linearity, GFS error of less than 4×10^{-5}%, maximum eddy current loss of 243 μW, and maximum of 8.45 kW ohmic power loss for all array elements. The maximum voltage across the terminals of all array elements is 74 V for the same 100 μs ramp-up time. A maximum field slew rate of 6940 T/m/s is achievable using available GPAs.

3.4 | Advanced mode: Shifted ROI with the same performance parameters

Another set of the optimized driving currents is computed to shift the ROI 60 mm along the z-axis keeping the gradient strength and field linearity intact. Figure 8 shows the B_z field plot, field sampling point for the GFS error assessment, and field transient response in this point. The simulations show the same RMS value of 87.6 A; gradient strength of 121 mT/m at the center of the shifted ROI; efficiency of 1.39 mT/m/A_{rms}; and 7.8% deviation from linearity within 70 mm diameter ROI, shifted 60 mm above the origin. The GFS error reads 7×10^{-4}% (the field transient response not shown). A maximum eddy power loss of 160 μW and a maximum of 8.6 kW ohmic power loss for all array elements are seen. The maximum voltage among all array elements is 83.9 V for the 100 μs rise time, which leads to a maximum available field slew rate of 3600 T/m/s.

3.5 | Advanced mode: Threefold higher gradient without shielding

An important key feature of the proposed active-shielded array coil compared to previous works[10–14] lies in its extra flexibility in adjusting the shield array functionality for specific applications. The extra degrees of freedom provided by the shield array elements can be used to provide very high gradient or slew rate for a short enough time such that the eddy effects can be ignored, or it may accompany the primary array to achieve a large ROI with a highly uniform but lower gradient strength and an acceptable shielding efficiency.

As a demonstration for extra flexibility, the shield array is fed in the reverse mode to increase the gradient strength up to threefold. Figure 9 shows the field map and the transient response for a new set of optimized currents with an RMS value of 86.0 A. About 7.6% deviation from linearity within the ROI of 120 mm diameter and a gradient strength of 376 mT/m can be seen. Due to intense induced eddy currents, the provided transient response shows 6.8×10^{-3}% GFS error that is about 3400 times higher compared to the standard mode of operation shown in Figure 4. Simulations (not shown here) show a maximum of 8.5 kW ohmic power loss in the array coils, a maximum of 14.8 W

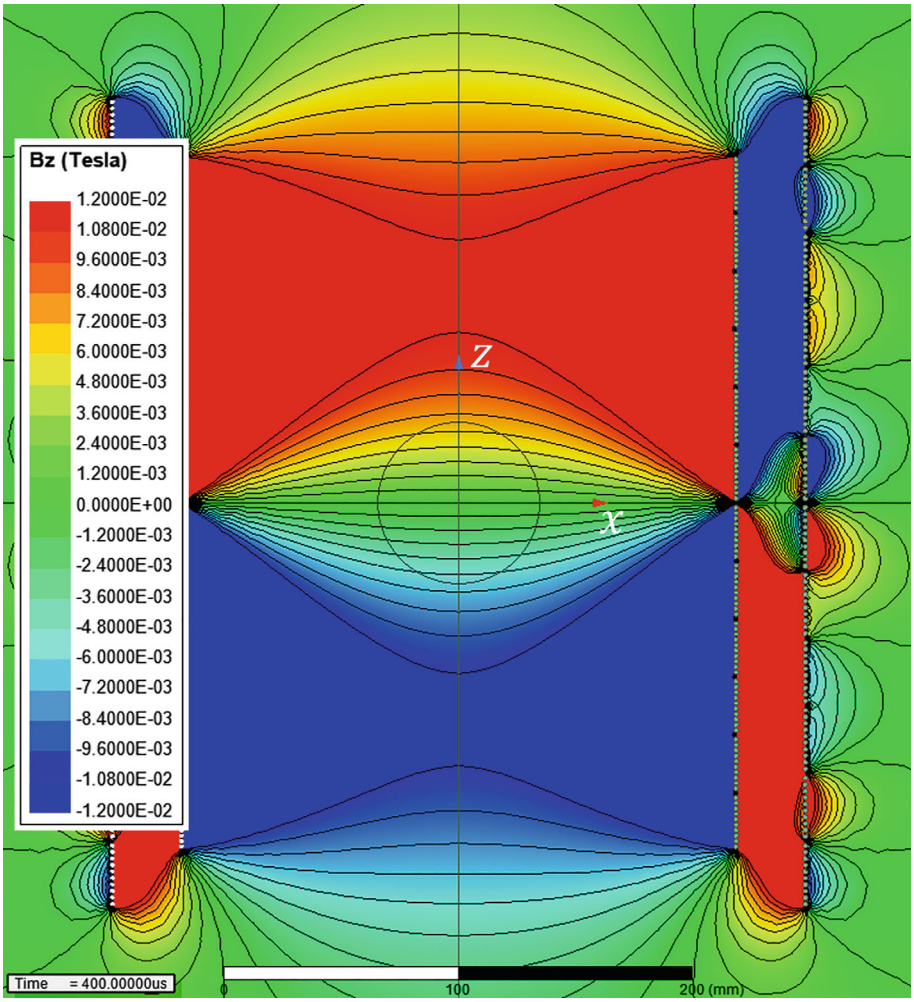

FIGURE 7 The B_z field plot of the proposed array, deployed in high gradient mode with the ROI at the center. The contour lines indicate 1.2 mT separations. A gradient strength of 206 mT/m with an efficiency of 2.36 $mT/m/A_{rms}$ and 8% deviation from linearity are achieved within the ROI of 70 mm diameter. The currents RMS is 87.3 A. The GFS error (transient response not shown) is less than 4×10^{-5}%.

power loss due to the eddy currents, and a maximum of 219.8 V among all array elements. In this case, the maximum field slew rate reaches to 3760 T/m/s for 100 μs ramp-up time. Although this amount of power loss can be tolerated by the cryogenic cooling system for a short enough time, it can be reduced by decreasing the slew rate. By increasing the current ramp-up time to 200 μs and 300 μs, the maximum power loss in the cryostat reduces to 10 W and 8.52 W, and the corresponding maximum voltages reduce to 113 and 77.1 V, respectively. It should be noted that the GFS error and the eddy current power loss will increase dramatically when the distance between the array elements and the cryostat decreases, which means that longer pulses should be used to prevent the quenching effect.

A magnetic profile with multiple ROIs is another significant feature of the proposed array in the advanced mode that is not shown in the results due to the article length limit. Simulation results and some experimental verification were shown for the unshielded array version in Ref.[7]. Furthermore, a simulation consisting of 2 (shiftable) ROIs is available for the active-shielded z-gradient array coil in Ref.[19]. More recently, in Ref.[20], multiple (shiftable) ROIs were reported based on a configuration similar to the current work, two of which are provided in the Supporting Information Figures S1-S2.

4 | DISCUSSION

The space dimension of the magnetic fluxes generated by all array elements is less than $N_C + N_S$ because those fields are not perpendicular to each other, neither within the ROI nor along the cryostat region. Based on a wide range of simulations not shown in this work, the following trade-offs have been observed between both $N_{C/S}$ and $M_{C/S}$ and the resulted field profile. (a) By increasing N_C, the resolution of adjustable performance parameters increases. This is similar to increase the number of shimming coils to achieve higher orders of spherical harmonics for more accurate shimming. (b) Increasing N_S improves the shielding effectiveness and provides better control to nullify the stray fields, especially when the ROI is shifted or a higher gradient is required. (c) Increasing M_C increases

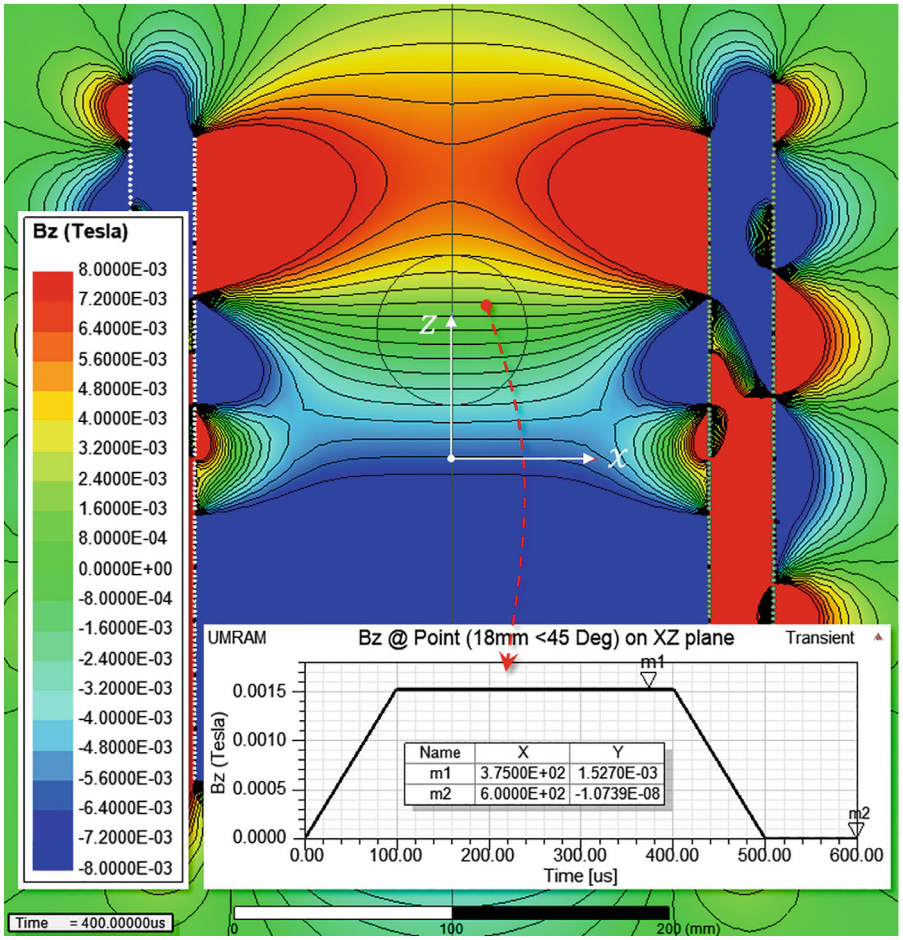

FIGURE 8 The B_Z field plot of the proposed array deployed in advanced mode, where the ROI is shifted 60 mm along the z-axis. The contour lines indicate 0.8 mT separations. The inset picture shows the field transient response at the field sampling point of 18 mm $< 45^{\circ}$ with respect to the center of the shifted ROI (shown by a tiny red circle). The gradient strength of 121 mT/m with an efficiency of 1.39 mT/m/A_{rms} and a 7.8% deviation from linearity is achieved within the ROI of 70 mm diameter. The RMS of currents is 86.7 A. The GFS error is about 7×10^{-4}%, which is low enough to ignore the eddy effects.

the gradient strength but reduces the resolution of feasible shifts and limits the dynamic range for the size of the ROI. (d) Increasing M_S provides better shielding but significantly increases the impedance of the shield array elements (compared to the primary array elements). The numbers we chose for different parameters mentioned in this work are collectively based on the above-mentioned trade-offs. Further investigations are required if the performance parameters or coil dimensions are changed.

Although the proposed array coils can change and shift the ROI only along the z-axis, similar methods based on the array concept[3] may be applied to yield similar results in other directions as well. This means that current MRI scanners can be upgraded to the array versions to deliver more sophisticated and advanced functionalities. The need for an advanced mode of operation that can adjust and localize the ROI(s) seems to draw more attention these days because of the diversity of new neuroscience applications and fMRI studies.

The proposed arrays can be controlled by a comprehensive look-up table for some predefined field profiles. However, it is more advantageous to use digital control algorithms (or even adaptive ones) to monitor the magnetic field on both the cryostat's surface and the inner surface of the RF coil (i.e., the closest physical surface to the ROI) to adjust the GPAs. Another benefit of an advanced digital driving system is its potential to achieve arbitrary nonlinear field profiles or nontraditional k-space traversing for modern gradient systems.

It is worth mentioning that comparing the efficiency of a conventional coil to that of an array coil might be misleading for two reasons: (a) The efficiency of the array coil is calculated using the RMS value of 24 independent currents (shown in Figures 3 and 6). Because there are so many constraints involved in designing an array coil, even a modest but marginal adjustment in one of them, such as greater linearity or reduced ohmic power loss, drastically impacts the distribution of those currents and hence the overall efficiency. (b) One of the most important constraints governing a conventional coil is that the current of all wires must be equal, regardless of whether they belong to the primary or shield coil or how far they are from the ROI. There is no such constraint in the array configuration that allows just enough current to be delivered wherever it is required. As our simulations show, such a freedom translates to a greater efficiency, that is, 1.95 mT/m/A_{rms} in the array design compared to 1.27 mT/m/A in the conventional design.

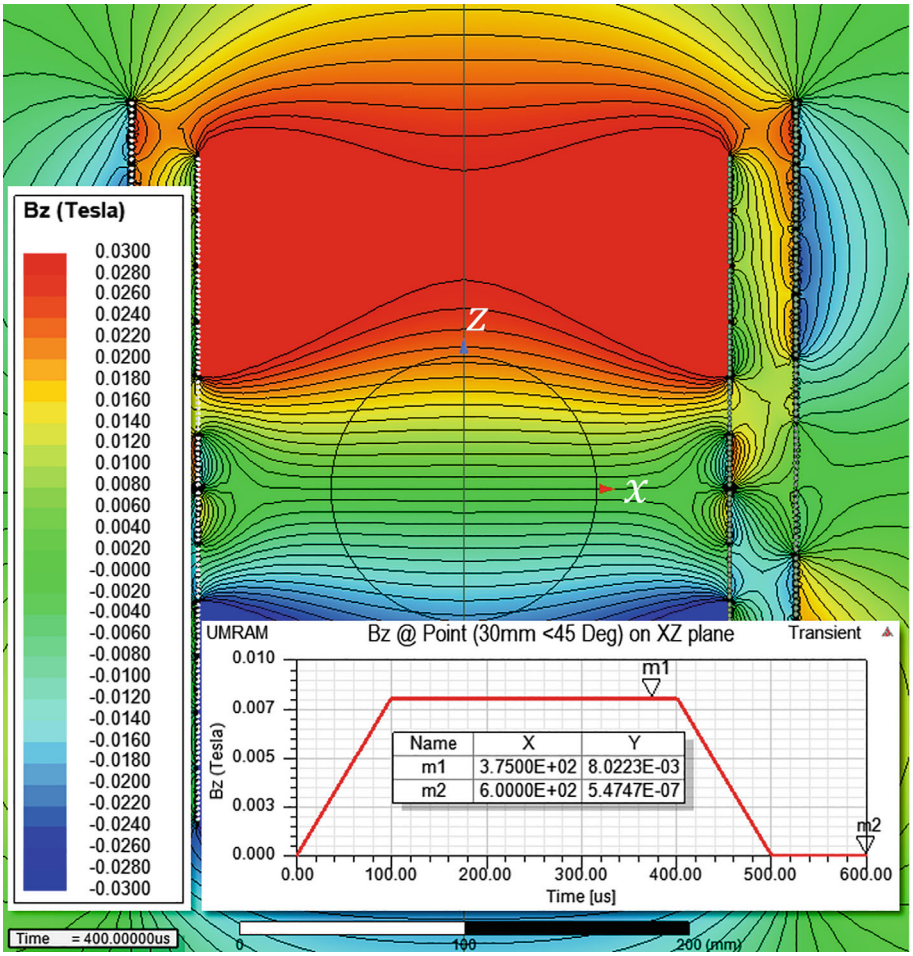

FIGURE 9 The B_z field plot of the proposed array deployed in the advanced mode, where threefold higher gradient strength is achieved with low shielding. The contour lines indicate 2 mT separations. The inset picture shows the field transient response at a point with a relative polar coordinate of 30 mm < 45°. The gradient strength of 376 mT/m and a 7.6% deviation from linearity are achieved within the ROI of 120 mm diameter. The RMS value for all feeding currents is 86.0 A. The GFS error is about 0.0068, that is, about 3400 times higher compared to the standard mode of operation shown in Figure 4.

Regarding the power consumption, as demonstrated in section 3.1, the total ohmic power loss for the proposed array in the standard mode is 4.1 kW, which is 13% less than the same-size conventional *z*-gradient coil of similar parameters (section 3.2). Regarding the advanced mode, the maximum power loss is 8.6 kW (the case with shifted ROI), which is 82% higher than the corresponding ohmic power loss of a conventional one. This is mainly because the conventional coils are optimized for minimum stored energy and/or minimum inductance[13] with fixed performance parameters. It is worth mentioning that array coils use multiple but less expensive GPAs compared to high-power GPAs used in conventional systems. Furthermore, because array elements have much less impedances (L + R) than the conventional design, turning on and off or switching between different configurations and modes would be considerably more agile. This can be verified by the values provided for the conventional coil, that is, 494 μH and 530 mΩ compared to the 59.8 μH and 58 mΩ for the shield array elements.

Finally, all possible mechanical design problems regarding the exerted forces and torques will be quite similar to the conventional designs with no further issues. This is also valid for the heat extraction subsystem because the power loss is in the same range (at most 40% higher for a short period of time).

5 | CONCLUSION

A modified optimization procedure based on analytic expressions is deployed to design and simulate an array-based *z*-gradient coil that consists of the primary array and its dedicated shield array. The performance of both arrays can be adjusted on the fly using a proper set of independent but programmable GPAs. The performance parameters such as the shape and position of the ROI, the gradient strength, and the linearity of the field can be adjusted. Commercial full-wave simulations are used to verify different modes of operations.

ORCID
Manouchehr Takrimi https://orcid.org/0000-0001-5515-2472
Ergin Atalar https://orcid.org/0000-0002-6874-6103

REFERENCES

1. Juchem C, Nixon TW, McIntyre S, Rothman DL, de Graaf RA. Magnetic field modeling with a set of individual localized coils. *J Magn Reson*. 2010;204:281-289.
2. Jia F, Littin S, Layton KJ, Kroboth S, Yu H, Zaitsev M. Desig of a shielded coil element of a matrix gradient coil. *J Magn Reson Imaging*. 2017;281:217-228.
3. Littin S, Jia F, Layton KJ, et al. Development and implementation of an 84-channel matrix gradient coil. *Magn Reson Med* 2018; 79:1181-1191.
4. Kroboth S, Layton KJ, Jia F, et al. Optimization of coil element configurations for a matrix gradient coil. *IEEE Trans Med Imaging* 2018; 37:284-292.
5. Smith E, Freschi F, Repetto M, Crozier S. The coil array method for creating a dynamic imaging volume. *Magn Reson Med*. 2017;78:784-793.
6. Jia F, Schultz G, Testud F, et al. Performance evaluation of matrix gradient coils. *MAGMA* 2016; 29:59-73.
7. Ertan K, Taraghinia S, Sadeghi A, Atalar E. A z-gradient array for simultaneous multi-slice excitation with a single-band RF pulse. *Magn Reson Med*. 2018;80:400-412.
8. Ertan K, Taraghinia S, Atalar E. Driving mutually coupled gradient array coils in magnetic resonance imaging. *Magn Reson Med*. 2019;82:1187-1198.
9. Ertan K, Taraghinia S, Sarıtas EU, Atalar E. Local optimization of diffusion encoding gradients using a z-gradient array for echo time reduction in DWI. In Proceedings of the 26th Annual Meeting of ISMRM, Paris, France, 2018.
10. Taraghinia S. *A z-Gradient Coil Array System for Magnetic Resonance Imaging* [Master Thesis]. Ankara, Turkey: Bilkent University; 2016. Accessed July 23, 2022. Available at: http://repository.bilkent.edu.tr/handle/11693/28988
11. Ertan NK. *Design and Applications of a z-Gradient Array in Magnetic Resonance Imaging* [PhD dissertation]. Ankara, Turkey: Bilkent University; 2019. Accessed July 23, 2022. Available at: http://repository.bilkent.edu.tr/handle/11693/48231
12. Paul CR. *Inductance: Loop and Partial*. John Wiley & Sons; 2010.
13. Hidalgo-Tobon S. Theory of gradient coil design methods for magnetic resonance imaging. *Concepts Magn Reson*. 2010;36A:223-242.
14. Maple 2021. *Maplesoft, a division of Waterloo Maple Inc., Maple 2021*, Waterloo, Ontario. Accessed July 28, 2022. Available at: https://www.maplesoft.com
15. Bi X, Park J, Deshpande V, Simonetti O, Laub G, Li D. Reduction of flow- and eddy-currents-induced image artifacts in coronary magnetic resonance angiography using a linear centric-encoding SSFP sequence. *Magn Reson Imaging*. 2007;25:1138-1147.
16. Takrimi M, Atalar E. MRI Hybrid Gradient Coil Equipped With a Programmable Z-Array and Conventional X- and Y- Elements. In Proceedings of the 29th Annual Meeting of the ISMRM, Virtual Conference, 2021:3099.
17. Babaloo R, Taraghinia S, Acikel V, Takrimi M, Atalar E, Digital Feedback Design for Mutual Coupling Compensation inGradient Array System. In Proceedings of the 28th Annual Meeting of ISMRM, Virtual Conference, 2020:4235.
18. Ansys, Inc. Website. Accessed July 28, 2022. Available at: https://www.ansys.com/products/electronics
19. Takrimi M, Atalar E. A Programmable Set of Z-Gradient Array and Active-Shield Array for Magnetic Resonance Imaging. In Proceedings of the 28th Annual Meeting of ISMRM, Virtual Conference, 2020:4242.
20. Takrimi M, Atalar E. Z-Gradient Array Coil Equipped With a Tunable Shield Array for Creating Multiple-Imaging Volumes. In Proceedings of the 31th Annual Meeting of ISMRM, London, UK, 2022. Accessed July 23, 2022. Available at: https://submissions.mirasmart.com/ISMRM2022/Itinerary/ConferenceMatrixEventDetail.aspx?ses=D-83. Abstract #1368

SUPPORTING INFORMATION

Additional supporting information may be found in the online version of the article at the publisher's website.

Figure S1. Two half cross-section B_Z field maps of the proposed array (with 0.2 mT contour lines) that generate double ROI configurations[20]: (a) Symmetric ROIs about the isocenter at ±7 cm; (b) the same ROIs shifted up by 2 cm. The cryostat is not shown for better magnification of the field details. (a) For 2 symmetric ROIs at ±7 cm, the diameter, linearity error, maximum gradient strength, and GFS error are 100 mm, 23.0%, 63 mT/m, and less than 2.4×10^{-4}%, respectively. The maximum RMS current for array elements is 42 A. (b) For the shifted version of (a) by 2 cm along the coil axis, the performance parameters are 100 mm, 24.8%, 62.3 mT/m, and 2.3×10^{-4}%, respectively. The RMS current is increased to 78.6 A.

Figure S2. The B_Z field maps of (a) three ROIs (0.2mT contours) and (b) five ROIs (0.1 mT contours) (20). (a) The gradient strengths are 58.9 mT/m at $z = 0$ and -60.4 mT/m at $z = \pm 8$ cm. The diameter, linearity error, and GFS error are 60 mm, less than 25.7%, and 1.0×10^{-4} % respectively. The RMS current is 81.2 A. (b) The gradient strengths are -22.2 mT/m at $z = 0$, 22.6 mT/m at $z = \pm 7$ cm, and -20.0 mT/m at $z = \pm 14$ cm. The diameter, linearity error, GFS error, and RMS current are 50 mm, between 23% and 27%, about 8.8×10^{-4} %, and 87.6 A, respectively.

How to cite this article: Takrimi M, Atalar E. A *z*-gradient array coil with a dedicated active-shielded array coil for MRI. *Magn Reson Med*. 2022;88:2718-2731. doi: 10.1002/mrm.29390